Optoelectronic Device Simulation of Bragg Reflectors and Their Influence on Surface Emitting Laser Characteristics

D.W. Winston,* *Member*, R.E. Hayes, *Member*

Department of Electrical and Computer Engineering
and the Optoelectronic Computing Systems Center
University of Colorado, Boulder CO, 80309-0425

Abstract

This paper presents a simulation analysis of distributed Bragg reflectors (DBRs) and their affect on the characteristics of vertical cavity surface emitting lasers (VCSELs). The SimWindows semiconductor device simulator models the close interaction between electrical, optical, and thermal processes present in VCSELs. This simulator is used to examine the electrical characteristics of some simple DBR designs. Due to the different transport characteristics of electrons and holes, these results will show that n-type DBR designs must be different than p-type designs in order to achieve the best operating characteristics for the overall laser. This analysis will demonstrate the improvement in the characteristics by comparing the simulation results of a standard VCSEL with the results of a VCSEL using improved DBR designs.

* Present address: IBM Microelectronics, E. Fishkill Facility, 1580 Route 52, Hopewell Junction NY, 12533

1. Introduction

Vertical Cavity Surface Emitting Lasers (VCSELs) are of growing interest in optoelectronics due to their potential use in 2D laser arrays, image processing, and optical communications systems. VCSELs function due to a complex interaction between electrical, optical, and thermal processes. Simulation can help separate this interaction and provide insight into the design of VCSELs. The SimWindows semiconductor device simulator models this interaction in various kinds of optoelectronic devices. It solves the electron and hole rate equations, the photon rate equation, and the lattice energy rate equation in one dimension. SimWindows enhances these standard models by adding quantum wells, Fermi-Dirac statistics, incomplete ionization, thermionic emission, tunneling, optical mode calculation, lateral heat flow, and temperature dependent material parameters (mobility, band gap, complex refractive index, and thermal conductivity). VCSEL simulations require all of these models in order to provide detailed results of the device operation. A summary of the SimWindows model appears in the Appendix while a complete description appears in [1].

Previous work on VCSEL modeling focused on thermal characteristics [2-5] where the electrical properties are principally based on phenomenological relations. Various optical formulations are either similar [6] or more advanced [7] than the SimWindows model, but again lack fundamental carrier and energy transport physics. One of the key components in the design of a good VCSEL is the distributed Bragg reflectors (DBRs). There is theoretical [8-10] and experimental [11-13] work on individual DBR structures. However, none have taken the approach of examining how specific DBR designs can influence the overall VCSEL characteristics.

This paper will present simulation results of individual DBR structures, and show how the

DBR design can influence the overall characteristics of VCSEL devices. Section 2 will discuss the general operation of a VCSEL and compare the best numerical result of a “standard” VCSEL with experimental results. This comparison will show that only when SimWindows uses all of the features in the model, can numerical results approximate experimental results. Section 3 will focus on the design of the DBR and propose structures that yield better DBR characteristics. This analysis will show that the design of the n-type and p-type DBRs must be independent from each other. A design that improves one DBR does not necessarily improve the other DBR. Section 4 will show simulation results of an “improved” VCSEL which incorporates the better DBR structures.

2. Standard VCSEL Design

A VCSEL operates by using two DBRs to reflect light across an active region. DBRs use layers of alternating material such that the optical path length is a quarter of the desired lasing wavelength. This yields very high reflectivities which VCSELs must use due to their short active region and overall cavity length. This is in comparison to edge emitting lasers that have a long active region and as a result can use comparatively small mirror reflectivities. One aspect of the short cavity length of VCSELs is that the wavelength spacing between adjacent resonant modes of the cavity is greater than in edge emitting lasers. VCSELs then lase at a single longitudinal mode determined by the optical characteristics of the structure. The VCSEL will emit light when the photon energy of the resonant wavelength coincides with an energy that the active region amplifies. If there is a mismatch between these energies, the device will not lase.

The disadvantage of using DBRs is that they are highly resistive and are the main cause of self-heating in VCSELs. Self heating causes the optical characteristics to change because both the refractive index and the band gap are temperature dependent. The change in the refractive index

typically causes the resonant frequency of the cavity to shift at approximately 0.8 Å/K, while the change in band gap causes the gain characteristics of the active region to shift at a rate of approximately 3.3 Å/K [15]. Since the wavelength shifting from these two effects is at different rates, a mismatch will occur between the resonant frequency and the gain characteristics. This mismatch decreases the light output beyond a specific current level. Reducing the resistance of the DBRs is necessary for reducing the heating in VCSELs and minimizing this effect.

Fig. 1 shows the equilibrium band diagram of a VCSEL structure that this section will refer to as the "standard" structure [14]. The active region consists of three undoped 10 nm GaAs quantum wells separated by 10 nm $Al_{0.16}Ga_{0.84}As$ barriers. The DBRs consist of alternating layers of 60.4 nm AlAs and 51.5 nm $Al_{0.16}Ga_{0.84}As$ with the left (top) DBR using 18 periods and the right (bottom) DBR using 28 periods. The DBRs also use 9.9 nm $Al_{0.58}Ga_{0.42}As$ "transition layers" between the thicker layers. These transition regions help reduce the resistance of the DBR by reducing the barriers to current flow in the conduction and valence bands. This configuration of layers yields the highest reflectivity at approximately 846 nm. The greater number of periods for the right DBR gives it a higher reflectivity than the left DBR. These simulations correspond to a reflectivity of 99.9% for the right DBR and 99.75% for the left DBR. The right DBR is doped n-type at a concentration of $3x10^{18}$ cm^{-3}. The left p-type DBR uses two doping sections. The shorter section closer to the contact is doped $2x10^{19}$ cm^{-3} with the longer section doped $5x10^{18}$ cm^{-3}. The left DBR also employs delta doping to reduce its resistance. Delta doping is an extra sheet charge at the interface between materials. The left DBR uses delta doping concentrations of $2.2x10^{12}$ cm^{-2} and $4.5x10^{12}$ cm^{-2} depending on the interface. These doping concentrations are high enough that free carrier absorption is significant, although SimWindows does not model free carrier absorption. Using the free carrier absorption coefficients in [16] and the computed carrier

concentrations from SimWindows, indicates that neglecting free carrier absorption in these VCSEL simulations represents approximately a 15% error in the mode gain of the VCSEL. These simulations also use a waveguide loss of 20 cm^{-1}.

To simulate lateral heat flow from the laser, SimWindows requires both the device radius and the environment radius. The device radius is 3.5 microns, and the environment radius, defined as the distance where the lattice temperature returns to a specified environment temperature, is 100 microns. These values were selected to model a single VCSEL surrounded by semiconductor material. For the thermal boundary conditions at the ends of the laser, the left contact uses a perfect thermal insulator and the right contact uses a finite thermal conductance of 1604.3 W cm^{-2} K^{-1}. This value results from an equation that assumes a small circular heat source in contact with a infinitely wide and infinitely thick layer of GaAs.

Fig. 2 shows a comparison between experimental [14] and numerical results for the standard VCSEL structure. It is important to note that the simulations only approximate experimental results when the simulator uses all of the physical effects in the model. In addition to solving the carrier rate equations, the photon rate equation, and the lattice energy rate equation, SimWindows uses Fermi-Dirac statistics, incomplete ionization, thermionic emission, tunneling, delta doping, temperature and doping dependent mobilities, temperature dependent band gap, temperature dependent thermal conductivity, and a temperature dependent refractive index. If the simulation does not use any one of these features, then the results change considerably. As stated earlier, the Appendix later in this paper gives a summary of the SimWindows model.

There are a number of factors that explain the deviation between the experimental results and the simulation. Including free carrier absorption would increase the simulated threshold current. A more accurate quantum well model would improve the coupling between the optical

and electrical equations. Both the simulation and the experimental results are on small area devices where two dimensional effects, not included here, play a role in the device characteristics. The structure of the simulated device is an ideal device obtained from a fabrication schedule, and fabrication variations would yield a device that differs from the specifications. Considering these factors, it is important to examine trends and comparisons in simulation results rather than specific values. The figures and discussion in this section will emphasize trends and show comparisons between simulation results.

Fig. 3 shows the light-current-voltage (LIV) characteristics at different environment temperatures. The curves labeled “300K” is the same numerical result shown in Fig. 2 except on a wider current scale. Since the gain of the laser is not only a direct function of temperature, but is also an indirect function of temperature through the band gap and resonant photon energy, an increase in the environment temperature causes both an increase in the threshold current and a decrease in the light output. Fig. 4 shows light-current (LI) plots for simulations using different physical models. Curves labeled “No Wavelength Shift” use a temperature independent refractive index. This keeps the lasing wavelength constant, but the temperature dependent band gap still causes the rollover characteristic where the optical power decreases with increasing current. Since both the band gap and the lasing wavelength shift towards lower energy, using a constant lasing wavelength in the simulations actually causes the rollover at a lower current level. Delta doping is one method to reduce the resistance of the p-type DBR. The characteristics in Fig. 4 improve when using delta doping because the VCSEL consumes less electrical power for a given current. This leads to less heating and a better match between the optical gain and the resonant photon energy of the cavity.

3. DBR Design

The design of the DBR is critical in determining the characteristics of the laser. Since the DBR uses a periodic structure, it is useful to analyze just one period of the DBR and then simulate the complete structure. As stated in the previous section, both DBRs in the standard VCSEL structure use 9.9 nm transition layers of $Al_{0.58}Ga_{0.42}As$ between longer layers of AlAs and $Al_{0.16}Ga_{0.84}As$. These do help reduce the resistance of the DBR, but it is not clear that a constant concentration of 58% aluminum is the optimum concentration. It is also not clear that this transition region has the same impact on the resistance in both the n-type and p-type DBRs. Various types of SimWindows simulations can address these issues.

Fig. 5 shows the electron current density through 1.5 periods of an n-type DBR and the hole current density through 1.5 periods of a p-type DBR as a function of the transition layer aluminum concentration. The bias on both structures is a constant 0.25 Volts. This figure shows that considerable barriers to electron flow exist at an aluminum concentration of 58% that the standard VCSEL structure uses. The peak electron current implying the lowest effective barrier height occurs at approximately 30% aluminum. This is in contrast to the hole current which peaks at approximately 60% aluminum. Even in a simple design where the transition layer aluminum concentration is constant, the design of the n-type and p-type DBRs should be different in order to reduce the resistance of both DBRs.

To understand the origin of the current profiles in Fig. 5, it is useful to plot the band profiles for a varying aluminum concentration in the transition regions. In the case of holes, Fig. 6 shows the valence band for 1.5 periods of a p-type DBR. The aluminum concentration of the 9.9 nm transition region ranges from 20% to 100%. The bias on this structure is again 0.25 Volts and Fig. 6 shows the direction of hole flow. Note that this figure plots the valence band in terms of the

hole energy, and so the holes flow down the valence band profile. This figure shows that the minimum barrier height does occur at approximately 60% aluminum with the maximum barrier height at both 20% and 100% aluminum.

Another question about DBR design is what other types of transition regions can yield yet smaller resistances. A second typical design is to use a linearly graded aluminum concentration rather than a constant intermediate concentration.

Fig. 7 compares the conduction bands and quasi-fermi levels for 1.5 periods of an n-type DBR using a constant 30% aluminum transition layer versus a 100% to 16% linearly graded aluminum transition layer. This figure clearly shows that the effective barriers to electron flow are greater for the linearly graded region than for the constant 30% region. This results in a larger voltage drop across the transition regions as illustrated by the larger change in quasi-fermi level in the linearly graded case than in the constant 30% case. The cause of the higher barriers in the linearly graded case is the decrease in the electron affinity between 100% and 50% aluminum concentration. When grading between 100% and 16% aluminum, the electron affinity actually decreases until the aluminum concentration reaches 50% and then the electron affinity increases again. This decrease produces the higher barriers seen in Fig. 7. The next issue is whether this result is true for p-type materials.

Fig. 8 compares the valence bands and quasi-fermi levels for 1.5 periods of a p-type DBR using a constant 60% aluminum transition layer versus a 100% to 16% linearly graded aluminum transition layer. The valence band in the 60% Al plot is a cross sectional slice of the surface plot in Fig. 6 except that Fig. 8 plots the electron energy. In this case, the linear grading drastically reduces the barrier height for holes. The combination of the electron affinity and the band gap favors linear grading over a constant transition layer. These two figures underscore the fact that a

design which improves one DBR may actually be detrimental to the other DBR.

The next step in this DBR analysis is to examine how the changes in the design of each period relates to improved electrical characteristics of the entire DBR. This section will now refer to the “improved” p-type DBR as a structure that uses a linearly graded transition layer while the “improved” n-type DBR uses a constant 30% aluminum transition layer.

Fig. 9 compares the simulated IV characteristics for the standard and improved designs of a 28 period n-type DBR. The improved design reduces the resistance by a factor of 3.3 from $7.7 \times 10^{-5}\ \Omega\ cm^2$ to $2.3 \times 10^{-5}\ \Omega\ cm^2$, but this figure shows that both designs still rely on tunneling through thin potential barriers because simulations without tunneling increases the resistance. Fig. 7 shows that these barriers are present with a 30% aluminum transition region. Fig. 10 shows similar IV characteristics for a 14 period p-type DBR. These characteristics differ from those in Fig. 9 in two ways. First, the reduction in resistance is by a factor of 7.1 from $1.5 \times 10^{-4}\ \Omega\ cm^2$ to $2.1 \times 10^{-5}\ \Omega\ cm^2$. Second, the improved p-type DBR design relies much less on tunneling current than both the standard p-type DBR design as well as either of the n-type DBR designs. Simulation results in Fig. 10 for the improved design show only a slight increase in resistance when neglecting tunneling current. This is a direct result of the linear grading region having a strong effect on the potential barriers as shown in Fig. 8.

4. Improved VCSEL Design

The last step in this analysis is to integrate the two improved DBR designs into a VCSEL structure and simulate the device. One aspect of the new DBR designs not mentioned in the previous section is the change in the optical characteristics resulting from the new transition layers. The linear grading of the transition layer in the improved p-type DBR does not have a

significant effect on the reflectivity of the DBR. The shift from a 58% to a 30% aluminum concentration in the improved n-type DBR transition layer does shift the reflectivity of the DBR to longer wavelengths. To counter this shift, the n-type DBR in the improved VCSEL uses a 9.4 nm instead of a 9.9 nm transition region. This keeps the optical path length of each period in the improved DBR the same as the standard DBR, and forces the resonant frequency of the cavity back to 846 nm. This change does not affect the selection of a 30% aluminum concentration transition region since it introduces a negligible change in the IV characteristics of the mirror.

Fig. 11 compares the LIV characteristics of the standard VCSEL structure with those of the improved VCSEL structure. The figures shows that by using the designs from the previous section, the improved device can generate higher peak optical powers than the standard device. This is a result of the lower resistance in the DBRs. At any given current, the device consumes less electrical power, there is less heating, and higher optical power. Fig. 12 compares the lattice temperature profiles of the standard and improved VCSEL structures. The optical power emitted by each device is 1.1 mW, but the improved device can emit this power at a much lower voltage. As a result, the electrical power dissipated by the device is less which yields a lower temperature.

5. Conclusions

This paper presented a simulation analysis of n- and p-type DBRs and their affect on VCSEL characteristics. Due to the different transport properties of electrons and holes, the two DBRs must be designed independently in order to minimize resistive heating in the VCSEL. This analysis is by no means an exhaustive analysis of VCSEL structures, but it serves to demonstrate the tight coupling between the electrical, optical, and thermal equations. The SimWindows simulator can help to analyze how specific design changes can affect both the individual component of a device as well as the complete device structure.

6. Appendix

$A^*_{n,p} = qm^*_{n,p}k^2 / 2p^2\hbar^3$	Electron and hole Richardson constants (A cm^{-2} K^{-2})
B	Spontaneous recombination constant (cm^3 s^{-1})
$\mathbf{D}$	Electrostatic Displacement (C cm^{-2})
E_c, E_v	Conduction and valence band edges (eV)
E_{fn}, E_{fp}	Electron and hole quasi-fermi levels (eV)
E_g	Band Gap (eV)
$E_{n,stim}$, $E_{p,stim}$	Electron and hole stimulated emission energies (eV)
$\mathcal{E}_{stim}$	Normalized stimulated electromagnetic field (cm$^{-3/2}$)
g, g_{max}	Local and maximum local gains (cm^{-1})
h	Planck Constant (6.626 x 10^{-34} J s)
$\mathbf{J}_n$, $\mathbf{J}_p$	Electron and hole current densities (A cm^{-2})
$\mathbf{J}^{therm}_{n,p\longrightarrow+}, \mathbf{J}^{therm}_{n,p+\rightarrow-}$	Electron and hole thermionic emission current densities (A cm^{-2})
$\mathbf{J}^{tun}_{n,p\longrightarrow+}, \mathbf{J}^{tun}_{n,p+\rightarrow-}$	Electron and hole tunneling current densities (A cm^{-2})
k	Boltzmann Constant (8.62 x 10^{-5} eV K^{-1})
m_n^*, m_p^*	Electron and hole density of states masses (kg)
n, p	Total electron and hole concentrations (cm^{-3})
n_i	Bulk intrinsic carrier concentration (cm^{-3})
N_D^+, N_A^-	Ionized donors and acceptor concentrations (cm^{-3})
q	Electronic charge (1.602 x 10^{-19} C)
r_d,r_e	Device and environment radii (cm)

S	Total number of photons in a mode (unitless)
$\mathbf{S}_n, \mathbf{S}_p$	Electron and hole energy fluxes (J cm^{-2} s^{-1})
$\mathbf{S}^{therm}_{n,p-\rightarrow+}, \mathbf{S}^{therm}_{n,p+\rightarrow-}$	Electron and hole thermionic emission energy fluxes (J cm^{-2} s^{-1})
$\mathbf{S}^{tun}_{n,p-\rightarrow+}, \mathbf{S}^{tun}_{n,p+\rightarrow-}$	Electron and hole tunneling energy fluxes (J cm^{-2} s^{-1})
$\mathbf{S}_{lat}$	Lattice energy flux (J cm^{-2} s^{-1})
T_L, T_n, T_p, T_{env}	Lattice, electron, hole, and environment Temperatures (K)
T_{rn}, T_{rp}	Electron and hole tunneling probabilities (unitless)
$U_{c-,v-}$	Conduction and valence band barrier heights (eV)
U_{tot}, U_{stim}, $U_{b\text{-}b}$, U_{srh}	Total, stimulated, spontaneous, and Shockley-Read-Hall recombination rates (cm^{-3} s^{-1})
$\tilde{U}_{stim}, \tilde{U}_{b-b}$	Total stimulated and spontaneous recombination rates integrated over the volume of the laser cavity (s^{-1})
v_{stim}	Velocity of stimulated emission photons (cm s^{-1})
W_{tot}	Total energy loss rate (J cm^{-3} s^{-1})
b	Fraction of spontaneous photons emitted into lasing mode (unitless)
$\in$	Dielectric permitivity (F cm^{-1})
$h_c = (E_{fn} - E_c)/kT_n$	Electron Planck potential (unitless)
$h_v = (E_v - E_{fp})/kT_p$	Hole Planck potential (unitless)
k, k_e	Material thermal conductivity and effective environment thermal conductivity (J s^{-1} cm^{-1} K^{-1})
m_n, m_p	Electron and hole mobilities (cm^2 V^{-1} s^{-1})

u_{stim}	Stimulated emission frequency (s^{-1})
r	Total Charge (C cm^{-3})
t_n, t_p	Electron and hole SHR recombination lifetimes (s)
t_{ph}	Photon lifetime (s)
f	Electrostatic Potential (V)

This Appendix provides a summary of the key equations that SimWindows uses to model VCSELs. Reference [1] gives a complete description of all the equations in SimWindows as well as a detailed explanation of the numerical solution techniques. SimWindows is fundamentally a one-dimensional drift-diffusion simulator that solves Poisson's equation, the current continuity equations, the photon rate equation, and the energy balance equation in steady state. It enhances these standard equations by adding quantum wells, Fermi-Dirac statistics, incomplete ionization, thermionic emission, tunneling, optical mode calculations, lateral heat flow, and temperature dependent material parameters (mobility, band gap, complex refractive index, and thermal conductivity). For simplicity, the equations in this Appendix assume 1) Boltzmann statistics 2) independent electron, hole, and lattice temperatures and 3) AlGaAs material system. However, the simulations results in this paper use Fermi-Dirac statistics and assume that the electrons, holes and lattice are in thermal equilibrium. Therefore, all three systems have the same local temperature which may vary over the length of the device.

SimWindows starts by solving Poisson's equation (1) and the current continuity equations (2). It includes a position dependent dielectric constant in the electric displacement expression (3) and incomplete ionization in total charge density expression (4).

$$\nabla \bullet \mathbf{D}(x) - r(x) = 0 \qquad (1)$$

$$\nabla \bullet (\mathbf{J}_n(x)/q) - U_{tot}(x) = 0 \quad \nabla \bullet (\mathbf{J}_p(x)/q) + U_{tot}(x) = 0 \tag{2}$$

$$\mathbf{D}(x) = -\in(x)\nabla f(x) \tag{3}$$

$$r(x) = q(p(x) - n(x) + N_D^+(x) - N_A^-(x)) \tag{4}$$

SimWindows models three types of current mechanisms. It applies drift-diffusion current (5,6) in regions where either the valence or conduction band changes continuously. The formulation below [17,18] includes gradients in both material parameters and temperature in addition to the usual terms for the electric field and carrier concentration gradients.

$$\mathbf{J_n} = m_n kT_n \nabla n + m_n n \nabla E_c - \tfrac{3}{2} m_n nkT_n \nabla \ln(m_n^*) + \tfrac{3}{2} m_n n \nabla kT_n \tag{5}$$

$$\mathbf{J}_p = -m_p kT_p \nabla p + m_p p \nabla E_v + \tfrac{3}{2} m_p pkT_p \nabla \ln(m_p^*) - \tfrac{3}{2} m_p p \nabla kT_p \tag{6}$$

Alternatively, SimWindows applies thermionic emission and tunneling current (7) where an abrupt change in the material causes a discontinuity in the valence or conduction bands [19].

$$\mathbf{J}_n = \mathbf{J}_{n-\to+}^{therm} - \mathbf{J}_{n+\to-}^{therm} + \mathbf{J}_{n-\to+}^{tun} - \mathbf{J}_{n+\to-}^{tun} \quad \mathbf{J}_p = \mathbf{J}_{p-\to+}^{therm} - \mathbf{J}_{p+\to-}^{therm} + \mathbf{J}_{p-\to+}^{tun} - \mathbf{J}_{p+\to-}^{tun} \tag{7}$$

In these equations, $- \to +$ signifies the current flowing from left to right and $+ \to -$ signifies current from right to left. The expressions for the thermionic emission (8) and tunneling currents (9) from left to right depend strictly on parameters on the left side of the band discontinuity. The equivalent expressions for current from right to left depend on parameters on the right side of the discontinuity:

$$\mathbf{J}_{n-\to+}^{therm} = -A_n^* T_{n-}^2 e^{h_{c-} - U_{c-}/kT_{n-}} \qquad \mathbf{J}_{p-\to+}^{therm} = A_p^* T_{p-}^2 e^{h_{v-} - U_{v-}/kT_{p-}} \tag{8}$$

$$\mathbf{J}_{n-\to+}^{tun} = -A_n^* \frac{T_{n-}}{k} \int_0^{U_{c-}} T_{rn}\left(E_x\right) e^{h_{c-} - E_x/kT_{n-}} dE_x \qquad \mathbf{J}_{p-\to+}^{tun} = A_p^* \frac{T_{p-}}{k} \int_0^{U_{v-}} T_{rp}\left(E_x\right) e^{h_{v-} - E_x/kT_{p-}} dE_x \tag{9}$$

where T_{rn} and T_{rp} are the electron and hole transmission probabilities that SimWindows computes using the WKB approximation [20].

For VCSEL simulations, SimWindows includes three recombination mechanisms: Shockley-Read-Hall (10), spontaneous emission (11), and stimulated emission (12).

$$U_{srh} = \frac{np - n_i^2}{(p + n_i)t_n + (n + n_i)t_p} \tag{10}$$

$$U_{b-b} = B(np - n_i^2) \tag{11}$$

$$U_{stim}(x) = v_{stim} g(x) S \left| \mathcal{E}_{stim}(x) \right|^2 \tag{12}$$

The equation for stimulated emission is very critical for simulating VCSEL devices. SimWindows uses a transmission matrix approach [21] with a temperature dependent complex refractive index to compute the electric field profile, $\mathcal{E}_{stim}(x)$, for the VCSEL structure. It also uses (13) and (14) to compute the local gain, $g(x)$, of the active region. These equations apply to bulk materials, but SimWindows uses similar equations for quantum wells [22].

$$g(hu_{stim}) = g_{max}(hu_{stim}) \left[f\left(\frac{E_{n,stim} - E_c}{kT_n} - h_c \right) - f\left(h_v - \frac{E_v - E_{p,stim}}{kT_p} \right) \right] \tag{13}$$

$$E_{n,stim} - E_c = \frac{m_p^*}{m_n^* + m_p^*}\left(hu_{stim} - E_g\right) \qquad E_v - E_{p,stim} = \frac{m_n^*}{m_n^* + m_p^*}\left(hu_{stim} - E_g\right) \tag{14}$$

The integral of the spontaneous and stimulated emission rates over the entire volume of the laser serve as the source terms for the photon rate equation (15). This equation balances the gain of photons from recombination with the loss of photons from emission out of the laser, scattering processes, etc. The photon lifetime, t_{ph}, accounts for these various loss mechanisms.

$$\tilde{U}_{stim} + b\tilde{U}_{b-b} - S/t_{ph} = 0 \tag{15}$$

To simulate the thermal properties of VCSELs, SimWindows solves the energy balance equation (16) assuming that the electrons and holes are in thermal equilibrium with the lattice. This equation relates the lattice, electron, and hole energy flux densities with the total loss of

energy due to photon emission.

$$\nabla \bullet (\mathbf{S}_{lat}(x) + \mathbf{S}_n(x) + \mathbf{S}_p(x)) + W_{tot}(x) = 0 \tag{16}$$

SimWindows uses (17) to compute the total lattice heat flux. The second term in this equation is an additional "lateral" heat flux that models the heat loss out the sides of the device. Without this term, accurate thermal simulations are impossible. This lateral heat flux model assumes a cylindrical device of radius r_d, surrounded by a cylindrical heat sink of radius r_e at an environment temperature of T_{env}. With this geometry, it is possible to derive an effective thermal conductivity, k_e, as a function of the actual thermal conductivity of the material (18).

$$\mathbf{S}_{lat} = -k(x)\nabla T_L \hat{\mathbf{x}} + \frac{\Delta x}{p r_d^2} k_e(x)(T_L(x) - T_{env})\hat{\mathbf{r}} \tag{17}$$

$$k_e(x) = k(x)\frac{2p}{\ln(r_e / r_d)} \tag{18}$$

The advantage of using this simple lateral heat flux model is that it acts simply as an additional heat loss term that depends on the local lattice temperature. SimWindows adds this heat loss term to the normal heat flowing through the device.

To complete the thermal flux model, SimWindows requires carrier energy flux expressions for each of the three current mechanisms. The electron and hole drift-diffusion energy fluxes are given in (19) and (20) respectively [18]. The electron and hole energy flux corresponding to thermionic emission and tunneling are given in (21-24). Again, combining these equations with the energy flux equations from left to right yields the total energy flux. Note that these equations are written for the total energy instead of just the kinetic energy, which is consistent with the definition of the total energy loss term defined in (25).

$$\mathbf{S}_n = -3m_n \frac{kT_n}{q}\left\{kT_n\nabla n + n\nabla E_c - \tfrac{3}{2}kT_n n\nabla \ln(m_n^*) + \tfrac{5}{2}n\nabla kT_n\right\} + \tfrac{E_c \mathbf{J}_n}{-q} \tag{19}$$

$$\mathbf{S}_p = -3\mu_p \frac{kT_p}{q}\left\{kT_p \nabla p - p\nabla E_v - \tfrac{3}{2}kT_p p\nabla \ln(m_p^*) + p\tfrac{5}{2}\nabla kT_p\right\} - \frac{E_v \mathbf{J}_p}{q} \tag{20}$$

$$\mathbf{S}_{n-\to+}^{therm} = \frac{A_n^* kT_{n-}^3}{q}\left(2 + \frac{U_{c-}}{kT_{n-}}\right)e^{\eta_{c-} - U_{c-}/kT_{n-}} + \frac{E_{c-}\mathbf{J}_{n-\to+}^{therm}}{-q} \tag{21}$$

$$\mathbf{S}_{p-\to+}^{therm} = \frac{A_p^* kT_{p-}^3}{q}\left(2 + \frac{U_{v-}}{kT_{p-}}\right)e^{\eta_{v-} - U_{v-}/kT_{p-}} - \frac{E_{v-}\mathbf{J}_{p-\to+}^{therm}}{q} \tag{22}$$

$$\mathbf{S}_{n-\to+}^{tun} = \frac{A_n^* T_{n-}^2}{q}\int_0^{U_{c-}} T_{rn}\left(E_x\right)\left(1 + \frac{E_x}{kT_{n-}}\right)e^{\eta_{c-} - E_x/kT_{n-}}\,dE_x + \frac{E_{c-}\mathbf{J}_{n-\to+}^{tun}}{-q} \tag{23}$$

$$\mathbf{S}_{p-\to+}^{tun} = \frac{A_p^* T_{p-}^2}{q}\int_0^{U_{v-}} T_{rp}\left(E_x\right)\left(1 + \frac{E_x}{kT_{p-}}\right)e^{\eta_{v-} - E_x/kT_{p-}}\,dE_x - \frac{E_{v-}\mathbf{J}_{p-\to+}^{tun}}{q} \tag{24}$$

The last term that (16) requires is the total energy loss from recombination, W_{tot} (25). Since SimWindows assumes that the electrons, holes and lattice are in thermal equilibrium, the energy loss only includes recombination processes that generate photons.

$$W_{tot} = \left(\tfrac{3}{2}kT_n + \tfrac{3}{2}kT_p + E_g\right)U_{b-b} + h\nu_{stim}U_{stim} \tag{25}$$

7. References

[1] D.W. Winston, "Physical Simulation of Optoelectronic Semiconductor Devices", Ph.D. Thesis, University of Colorado at Boulder, June, 1996. The latest version of SimWindows is available at http://www-ocs.colorado.edu/SimWindows/simwin.html

[2] G.R. Hadley, K.L. Lear, M.E. Warren, K.D. Choquette, J.W. Scott, and S.W. Corzine, "Comprehensive Numerical Modeling of Vertical-Cavity Surface-Emitting Lasers," *IEEE Journal of Quantum Electron*., Vol. 32, pp. 607-616, April 1996.

[3] W. Nakwaski, and M. Osinski, "Thermal Properties of Etched-Well Surface-Emitting Semiconductor Lasers," *IEEE Journal of Quantum Electron*., Vol. 27, pp. 1391-1401, June 1991.

[4] W. Nakwaski, and M. Osinski, "Thermal Analysis of GaAs-AlGaAs Etched-Well Surface-Emitting Double-Heterostructure Lasers with Dielectric Mirrors," *IEEE Journal of Quantum Electron*., Vol. 29, pp. 1981-1995, June 1993.

[5] J.W. Scott, R.S. Geels, S.W. Corzine, and L.A. Coldren, "Modeling Temperature Effects and Spatial Hole Burning to Optimize Vertical-Cavity Surface-Emitting Laser Performance," *IEEE Journal of Quantum Electron*., Vol. 29, pp. 1295-1308, May 1993.

[6] R. Michalzik, and K.J. Ebeling, "Modeling and Design of Proton-Implanted Ultralow-Threshold Vertical-Cavity Laser Diodes," *IEEE Journal of Quantum Electron*., Vol. 29, pp. 1963-1974, June 1993.

[7] R. Michalzik, and K.J. Ebeling, "Quasi-3D Modeling of Vertical-Cavity Surface Emitting

Laser Operation," *Proc. SPIE's Physics and Sim. of Optoelectron. Dev. III*, San Jose CA, Feb. 6-9, pp. 360-371, 1995.

[8] S.S. Yechuri, T.-J.B. Shieh, and R.H. Johnson, "Design of Flat-Band AlGaAs Heterojunction Bragg Reflectors," *IEEE Trans. Electron Dev.*, Vol. 43, pp. 40-46, Jan. 1996.

[9] R.F. Nabiev, and C.J. Chang-Hasnain, "Voltage Drop in n- and p-Type Bragg Reflectors for Vertical-Cavity Surface-Emitting Lasers," *IEEE Phot. Tech. Let.*, Vol. 7, pp. 733-735, July 1995.

[10] E. Zeeb, and K.J. Ebeling, "Potential Barriers and Current-Voltage Characteristic of p-Doped Graded AlAs-GaAs heterojunctions," *J. Appl. Phys.*, Vol. 72, pp. 993-999, Aug. 1, 1992.

[11] K.Kurihara, T. Numai, I. Ogura, A. Yasuda, M. Sugimoto, and K. Kasahara, "Reduction in the Series Resistance of the Distributed Bragg Reflector in Vertical Cavities by Using Quasi-Graded Superlattices at the Heterointerfaces," *J. Appl. Phys.*, Vol. 73, pp. 21-27, Jan. 1, 1993.

[12] R.F. Kopf, E.F. Schubert, S.W. Downey, and A.B. Emerson, "N- and P-type Dopant Profiles in Distributed Bragg Reflector Structures and Their Effect on Resistance," *Appl. Phys. Lett.*, Vol. 61, pp. 1820-1822, Oct. 12, 1992.

[13] K. Tai, L. Yang, Y.H. Wang, H.D. Wynn, and A.Y. Cho, "Drastic Reduction of Series Resistance in Doped Semiconductor Distributed Bragg Reflectors for Surface-Emitting Lasers," *Appl. Phys. Lett.*, Vol. 56, pp. 2496-2498, June 18, 1990.

[14] Structure and experimental data provided by H. Temkin, Colorado State University.

[15] D.B. Young, J.W. Scott, F.H. Peters, B.J. Thibeault, S.W. Corzine, M.G. Peters, S.-L. Lee, and L.A. Coldren, "High-Power Temperature-Insensitive Gain-Offset InGaAs/GaAs Vertical-Cavity Surface-Emitting Lasers,"*IEEE Phot. Tech. Let*., Vol. 5, pp. 129-132, Feb. 1993.

[16] G. Tan, N. Bewtra, K. Lee, and J.M. Xu, "A Two-Dimensional Nonisothermal Finite Element Simulation of Laser Diodes,"*IEEE Journal of Quantum Electron*., Vol. 29, pp. 822-835, March 1993.

[17] A.H. Marshak, and K.M. van Vliet, "Electrical Current in Solids with Position-Dependent Band Structure,"*Solid State Electron*., Vol. 21, pp. 417-427, 1978.

[18] Y. Apanovich, P. Blakey, R. Cottle, E. Lyumkis, B. Polsky, A. Shur, and A. Tcherniaev, "Numerical Simulation of Submicrometer Devices Including Coupled Nonlocal Transport and Nonisothermal Effects,"*IEEE Trans. Electron Dev.*, Vol. 42, pp. 890-898, May 1995.

[19] K. Yang, J.R. East, and G.I. Haddad, "Numerical Modeling of Abrupt Heterojunctions Using a Thermionic-Field Emission Boundary Condition,"*Solid State Electron*., Vol. 36, pp. 321-330, 1993.

[20] C.B. Duke,*Tunneling in Solids*, Academic Press NY, 1969.

[21] B.-G. Kim, and E. Garmire, "Comparison Between the Matrix Method and the Coupled-Wave Method in the Analysis of Bragg Reflector Structures,"*Journ. Opt. Soc. Am.*, Vol. 9, pp. 132-136, Jan. 1992.

[22] P.S. Zory Jr. ed.,*Quantum Well Lasers*, Academic Press NY, 1993.

8. Figure Captions

Fig. 1. Equilibrium band diagram for a standard VCSEL

Fig. 2. Experimental and simulated results for the “standard” VCSEL structure

Fig. 3. LIV characteristics for the standard VCSEL at different environment temperatures

Fig. 4. LI plots for combinations of delta doping and wavelength shifting

Fig. 5. Electron and hole current through 1.5 periods of an n-type and p-type DBR for various transition region aluminum concentrations

Fig. 6. Valence band of 1.5 periods of a DBR for different transition layer concentrations (note that z axis is hole energy)

Fig. 7. Conduction bands and electron quasi-fermi levels for 1.5 periods of an n-type DBR using 30% and linear graded transition regions

Fig. 8. Valence bands and hole quasi-fermi levels for 1.5 periods of a p-type DBR using 60% and linear graded transition regions

Fig. 9. IV comparisons of the improved versus standard n-type DBR design

Fig. 10. IV Comparisons of the improved versus standard p-type DBR design

Fig. 11. LIV characteristics for the standard and improved VCSEL

Fig. 12. Temperature profiles for the standard and improved VCSEL at 1.1 mW optical power

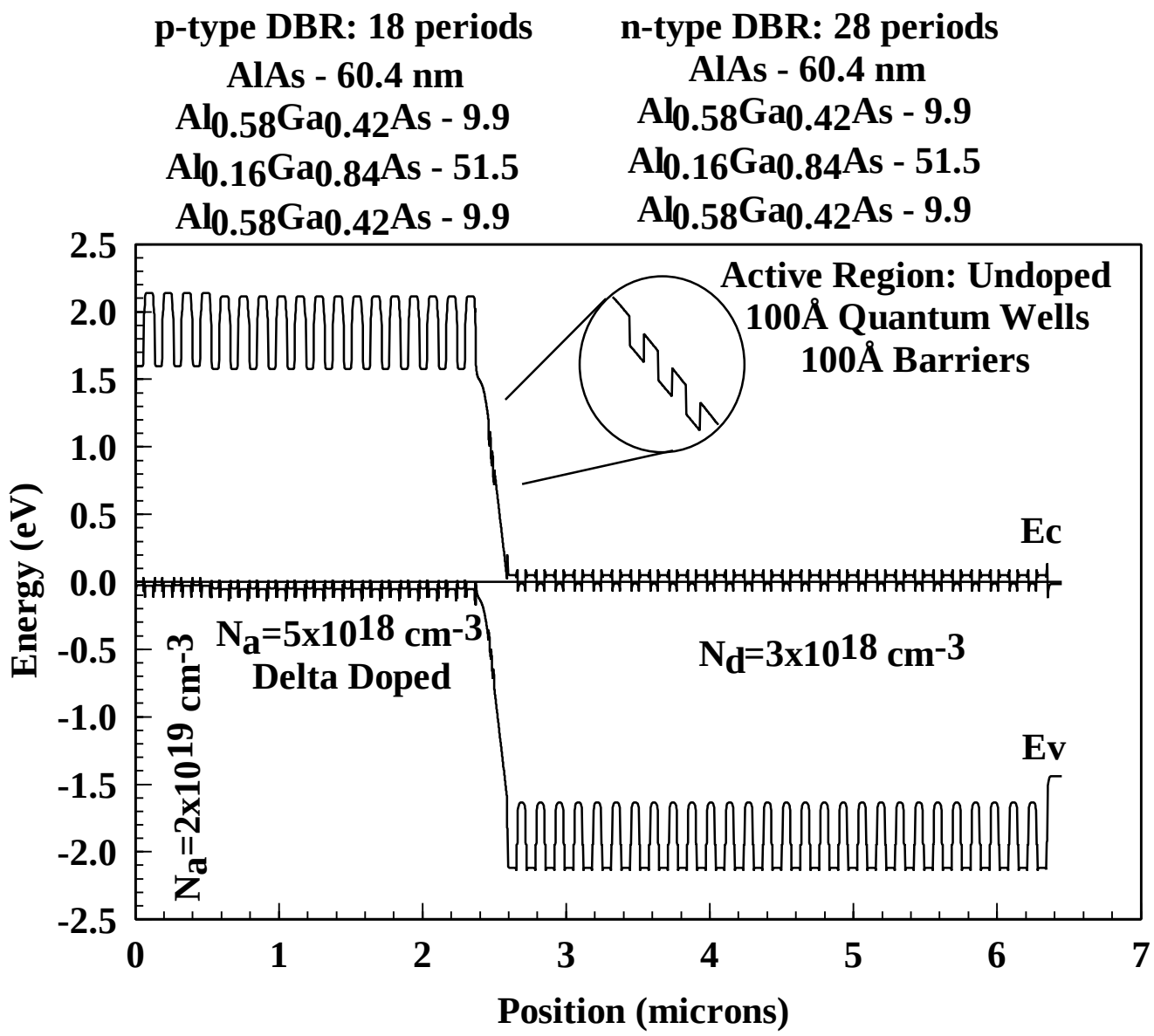
p-type DBR: 18 periods
AlAs - 60.4 nm
Al0.58Ga0.42As - 9.9
Al0.16Ga0.84As - 51.5
Al0.58Ga0.42As - 9.9
n-type DBR: 28 periods
AlAs - 60.4 nm
Al0.58Ga0.42As - 9.9
Al0.16Ga0.84As - 51.5
Al0.58Ga0.42As - 9.9
Active Region: Undoped
100Å Quantum Wells
100Å Barriers
Ec
Ev
Na=5x10^18 cm^-3
Delta Doped
Na=2x10^19 cm^-3
Nd=3x10^18 cm^-3
Energy (eV)
Position (microns)
2.5
2.0
1.5
1.0
0.5
0.0
-0.5
-1.0
-1.5
-2.0
-2.5
0
1
2
3
4
5
6
7

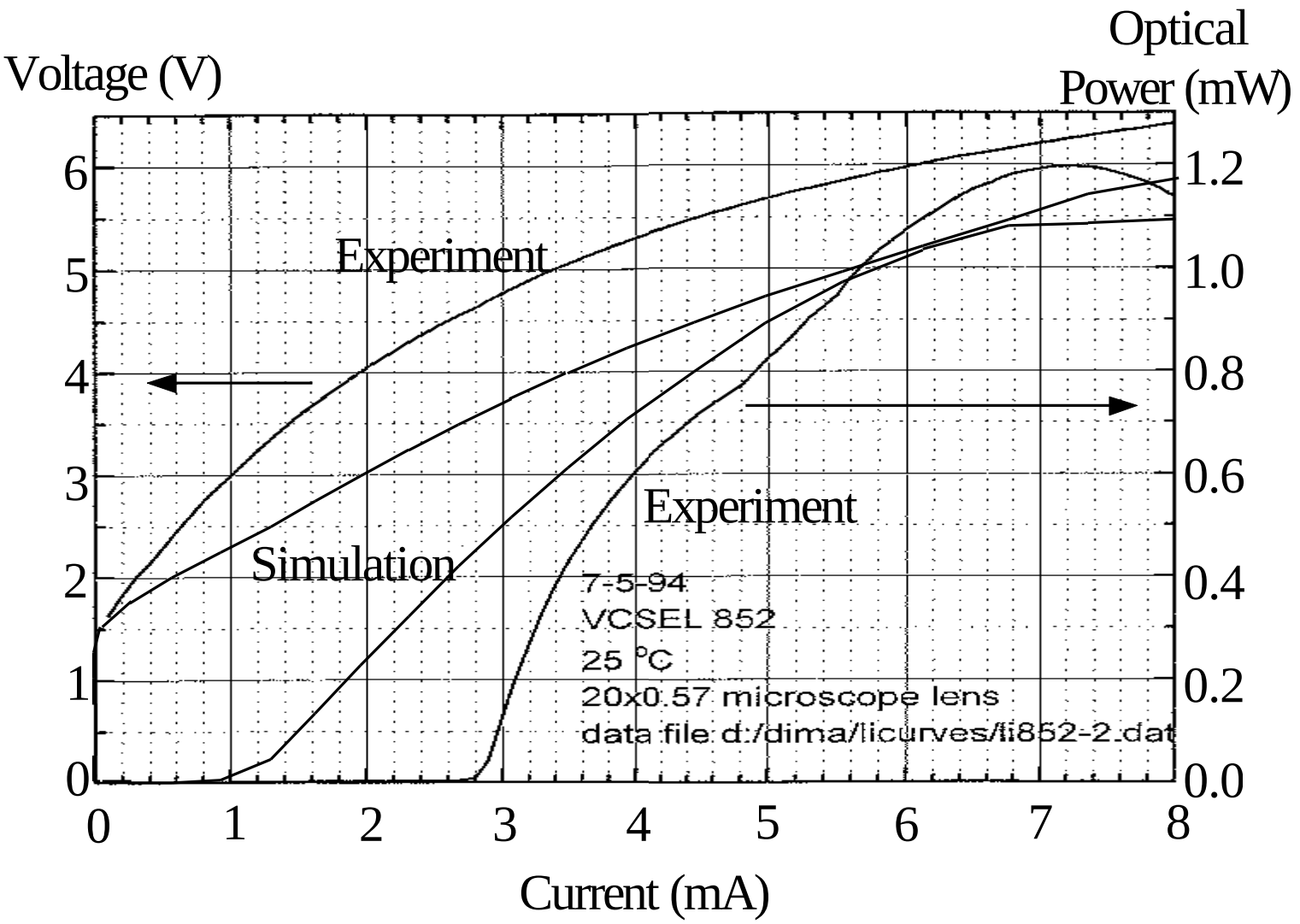
Voltage (V)
Optical
Power (mW)
Experiment
Simulation
Experiment
7-5-94
VCSEL 852
25 °C
20x0.57 microscope lens
data file d:/dima/licurves/li852-2.dat
0
1
2
3
4
5
6
0.0
0.2
0.4
0.6
0.8
1.0
1.2
0
1
2
3
4
5
6
7
8
Current (mA)

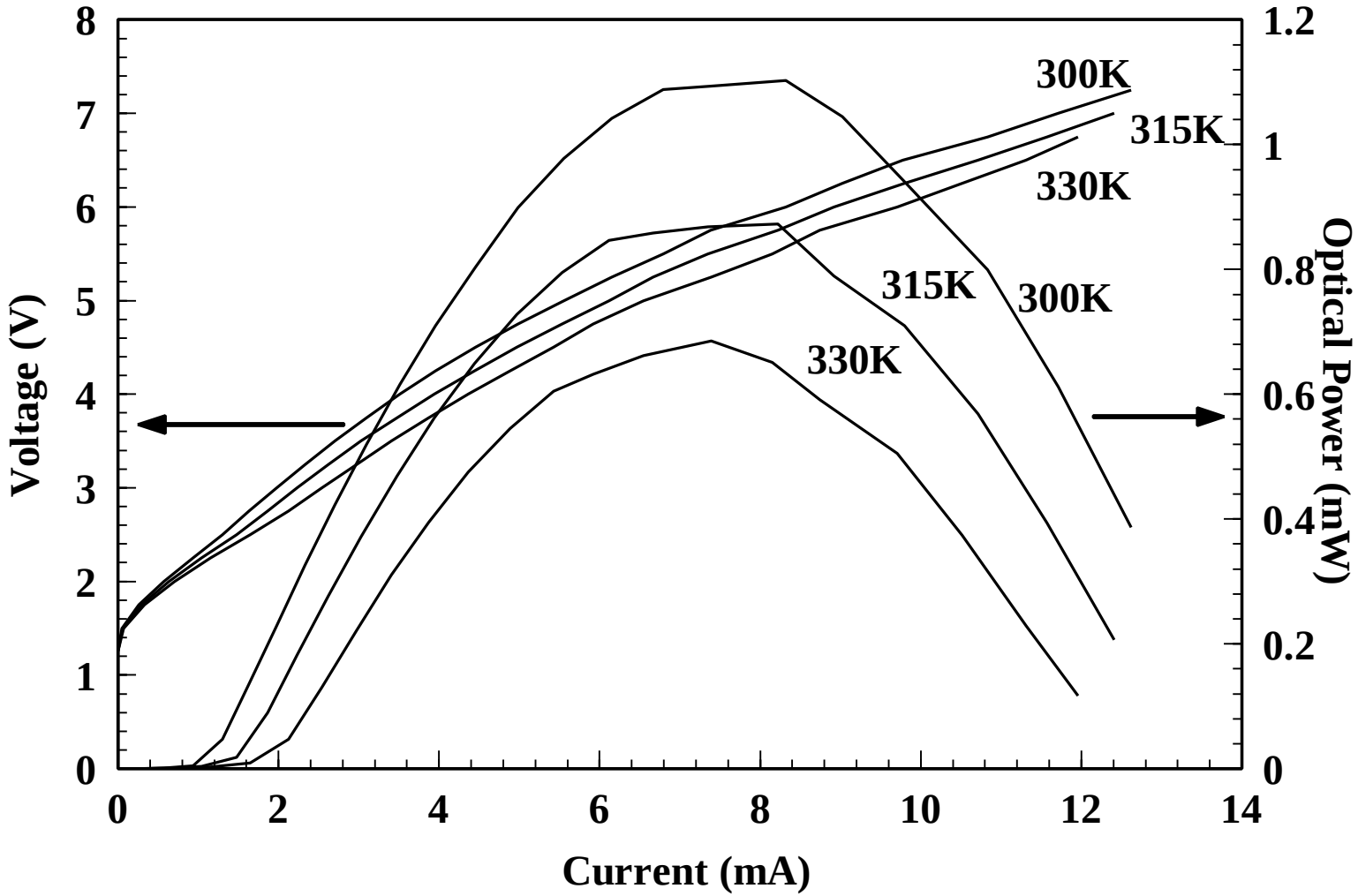
Voltage (V)
Optical Power (mW)
Current (mA)
300K
315K
330K
315K
300K
330K
0
1
2
3
4
5
6
7
8
0
0.2
0.4
0.6
0.8
1
1.2
0
2
4
6
8
10
12
14

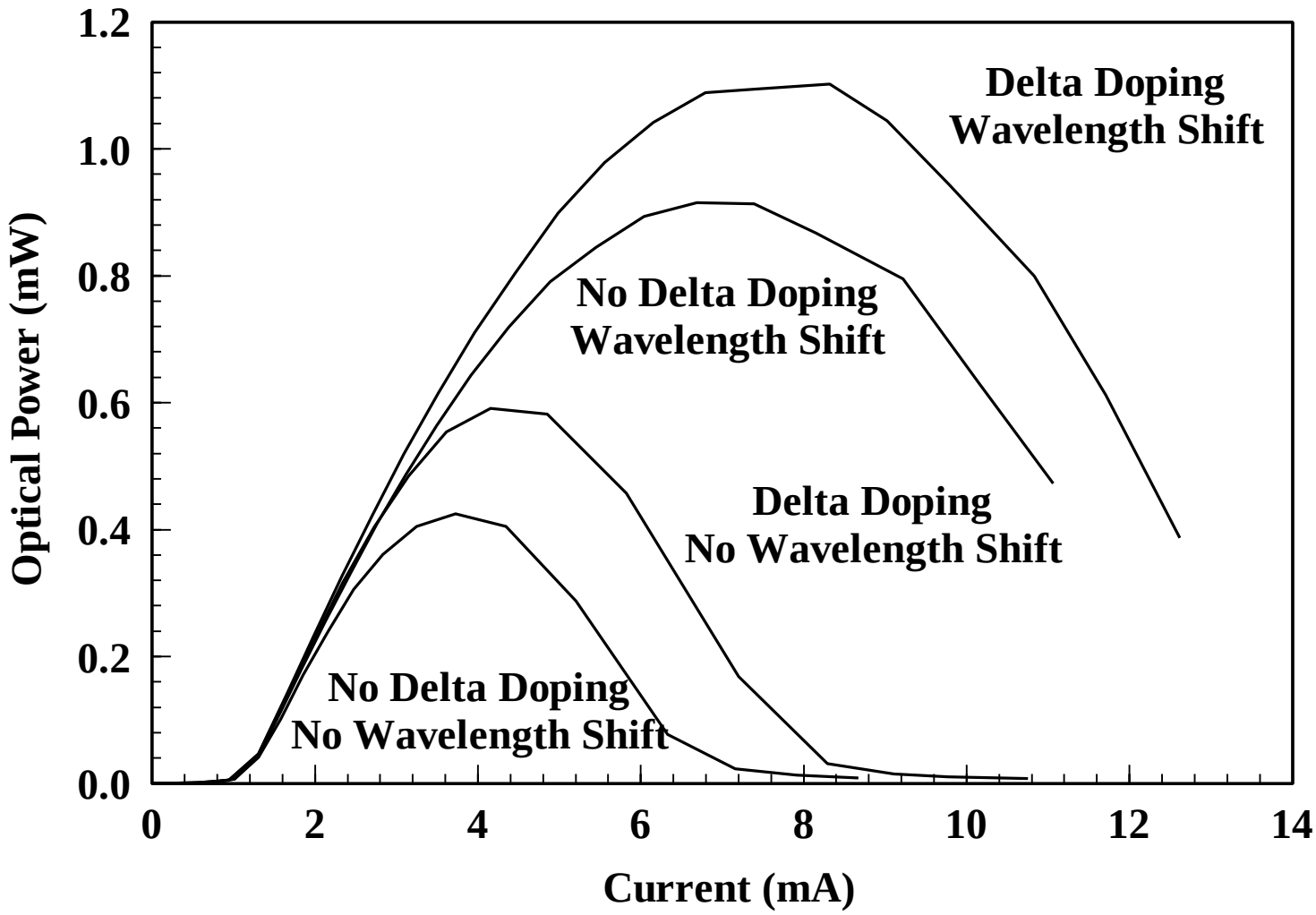
Optical Power (mW)
1.2
1.0
0.8
0.6
0.4
0.2
0.0
0
2
4
6
8
10
12
14
Current (mA)
Delta Doping
Wavelength Shift
No Delta Doping
Wavelength Shift
Delta Doping
No Wavelength Shift
No Delta Doping
No Wavelength Shift

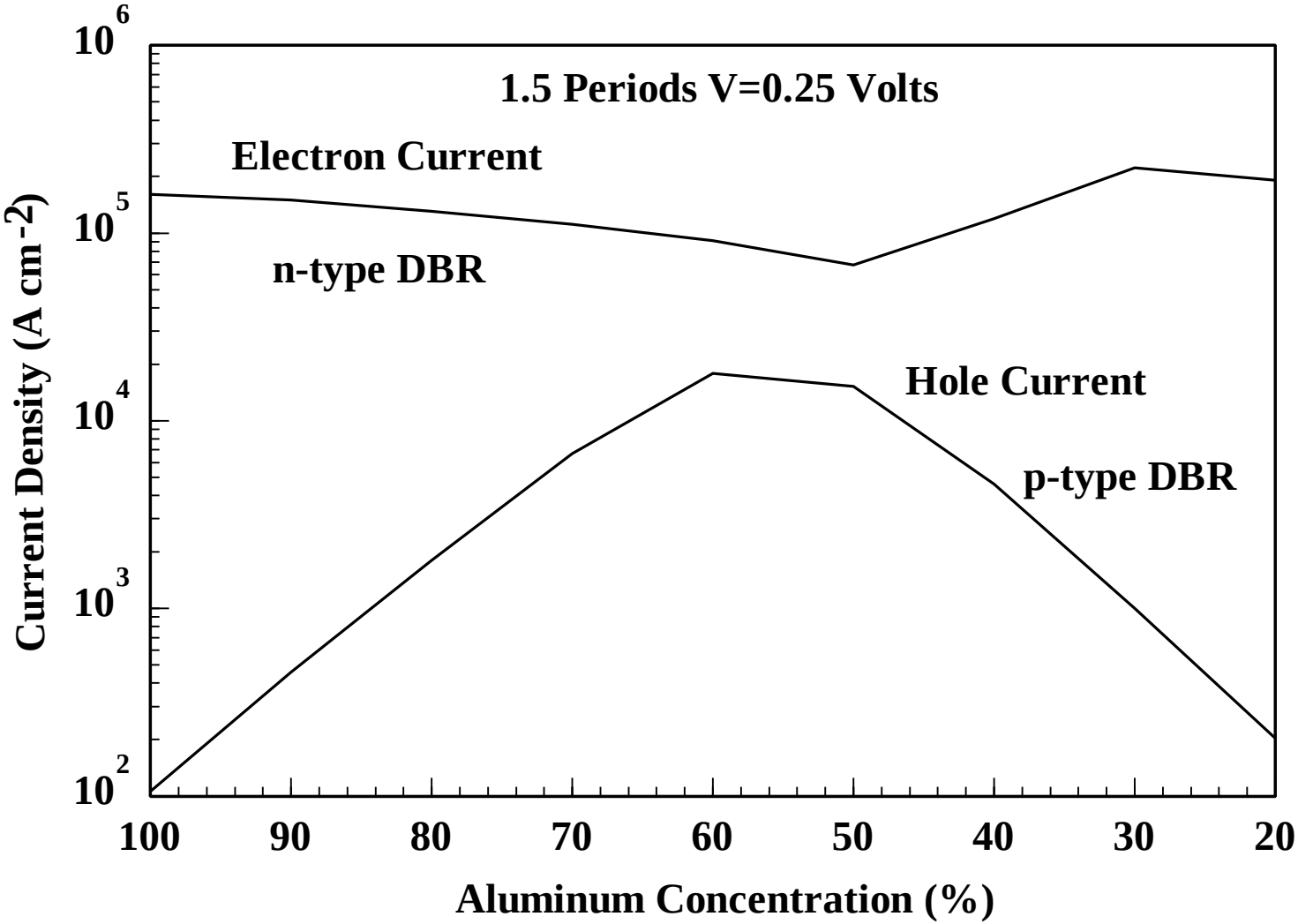
1.5 Periods V=0.25 Volts
Electron Current
n-type DBR
Hole Current
p-type DBR
Current Density (A cm-2)
10^6
10^5
10^4
10^3
10^2
100
90
80
70
60
50
40
30
20
Aluminum Concentration (%)

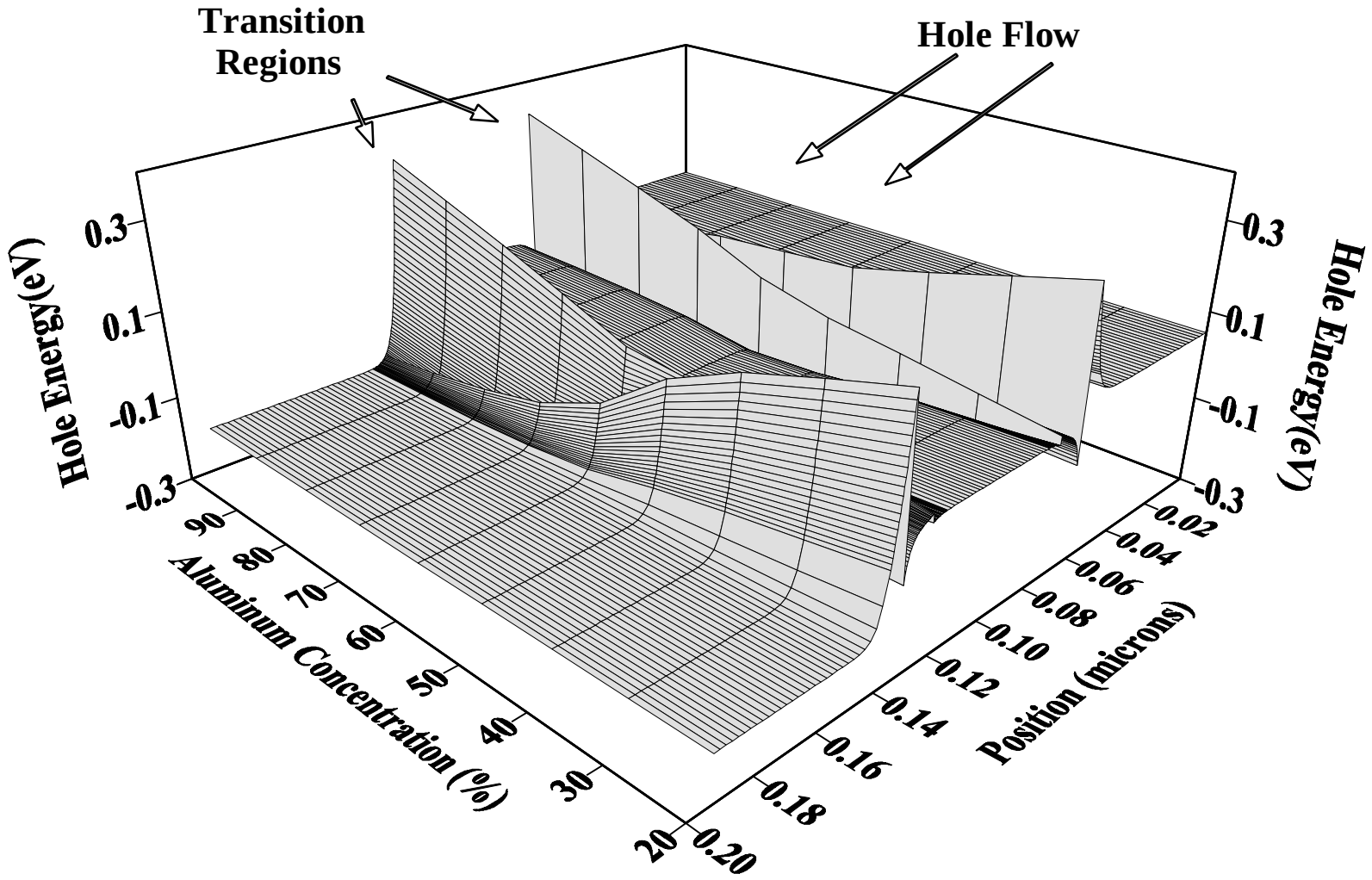
Transition Regions
Hole Flow
Hole Energy(eV)
0.3
0.1
-0.1
-0.3
90
80
70
60
50
40
30
20
Aluminum Concentration (%)
0.20
0.18
0.16
0.14
0.12
0.10
0.08
0.06
0.04
0.02
Position (microns)
Hole Energy(eV)
0.3
0.1
-0.1
-0.3

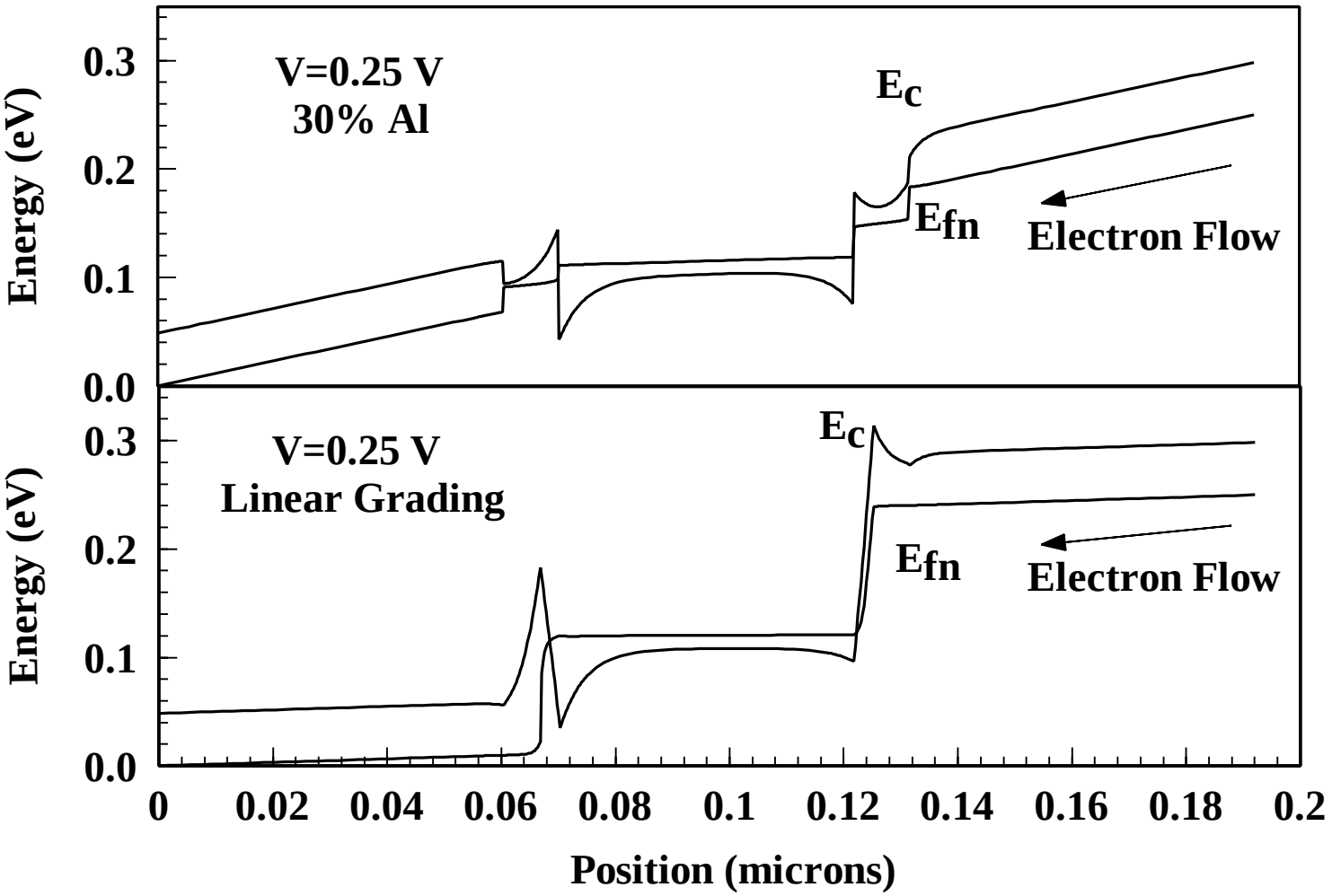
V=0.25 V
30% Al
E_c
E_{fn}
Electron Flow
Energy (eV)
0.0
0.1
0.2
0.3
V=0.25 V
Linear Grading
E_c
E_{fn}
Electron Flow
Energy (eV)
0.0
0.1
0.2
0.3
0
0.02
0.04
0.06
0.08
0.1
0.12
0.14
0.16
0.18
0.2
Position (microns)

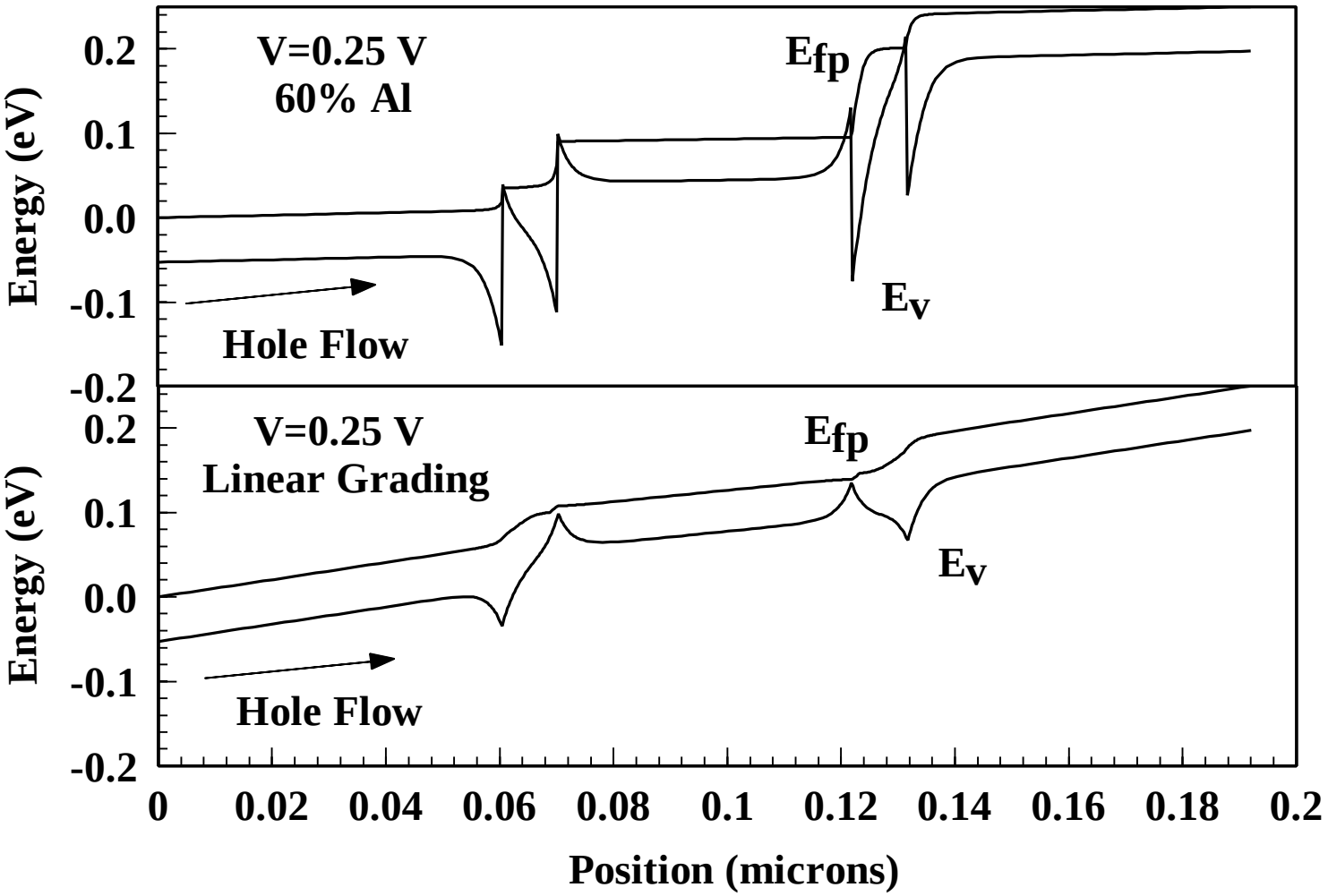
V=0.25 V
60% Al
E_{fp}
E_v
Hole Flow
Energy (eV)
V=0.25 V
Linear Grading
E_{fp}
E_v
Hole Flow
Energy (eV)
0.2
0.1
0.0
-0.1
-0.2
0
0.02
0.04
0.06
0.08
0.1
0.12
0.14
0.16
0.18
0.2
Position (microns)

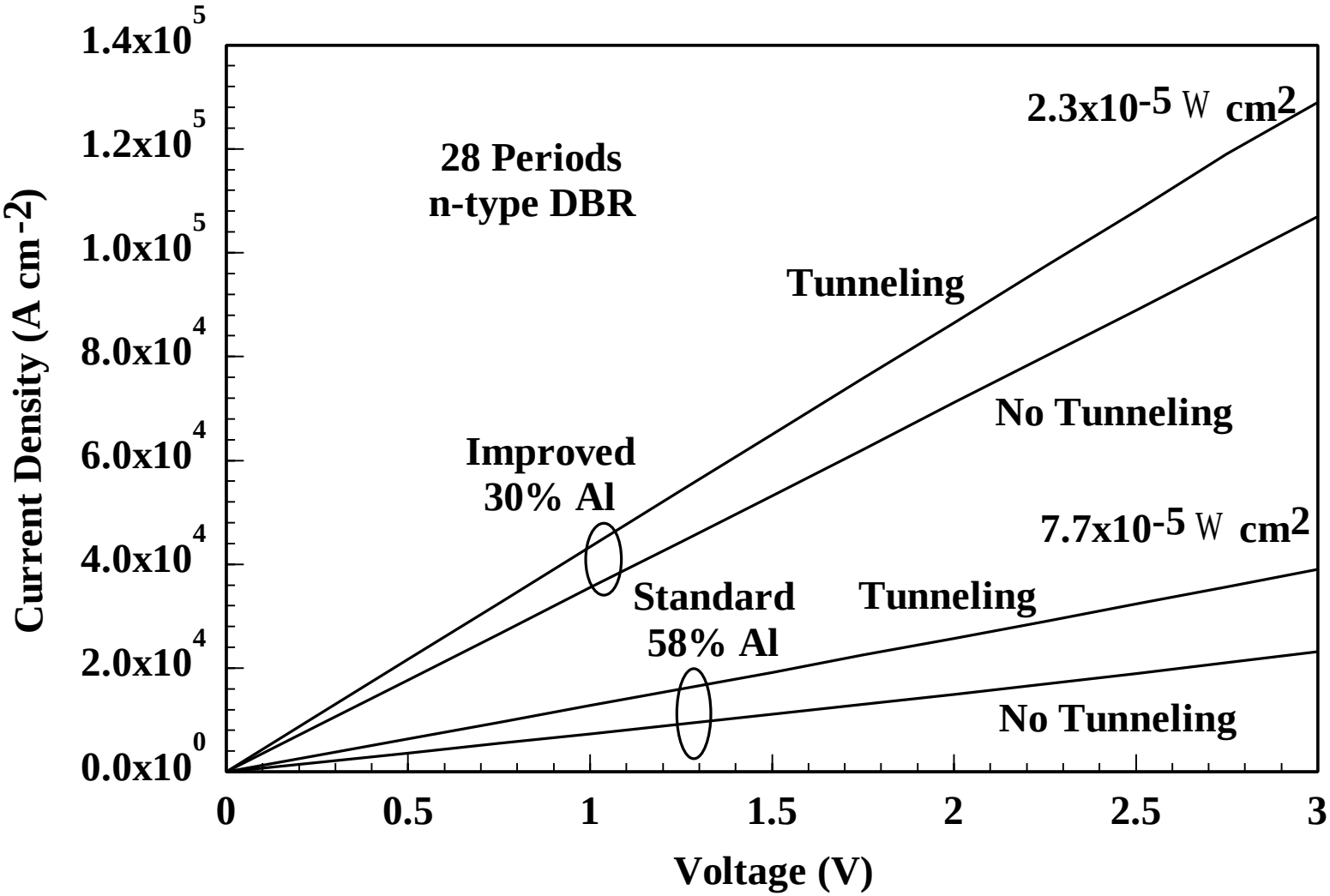
1.4x10^5
1.2x10^5
1.0x10^5
8.0x10^4
6.0x10^4
4.0x10^4
2.0x10^4
0.0x10^0
Current Density (A cm^-2)
0
0.5
1
1.5
2
2.5
3
Voltage (V)
28 Periods
n-type DBR
2.3x10^-5 W cm^2
Tunneling
No Tunneling
Improved
30% Al
7.7x10^-5 W cm^2
Standard
58% Al
Tunneling
No Tunneling

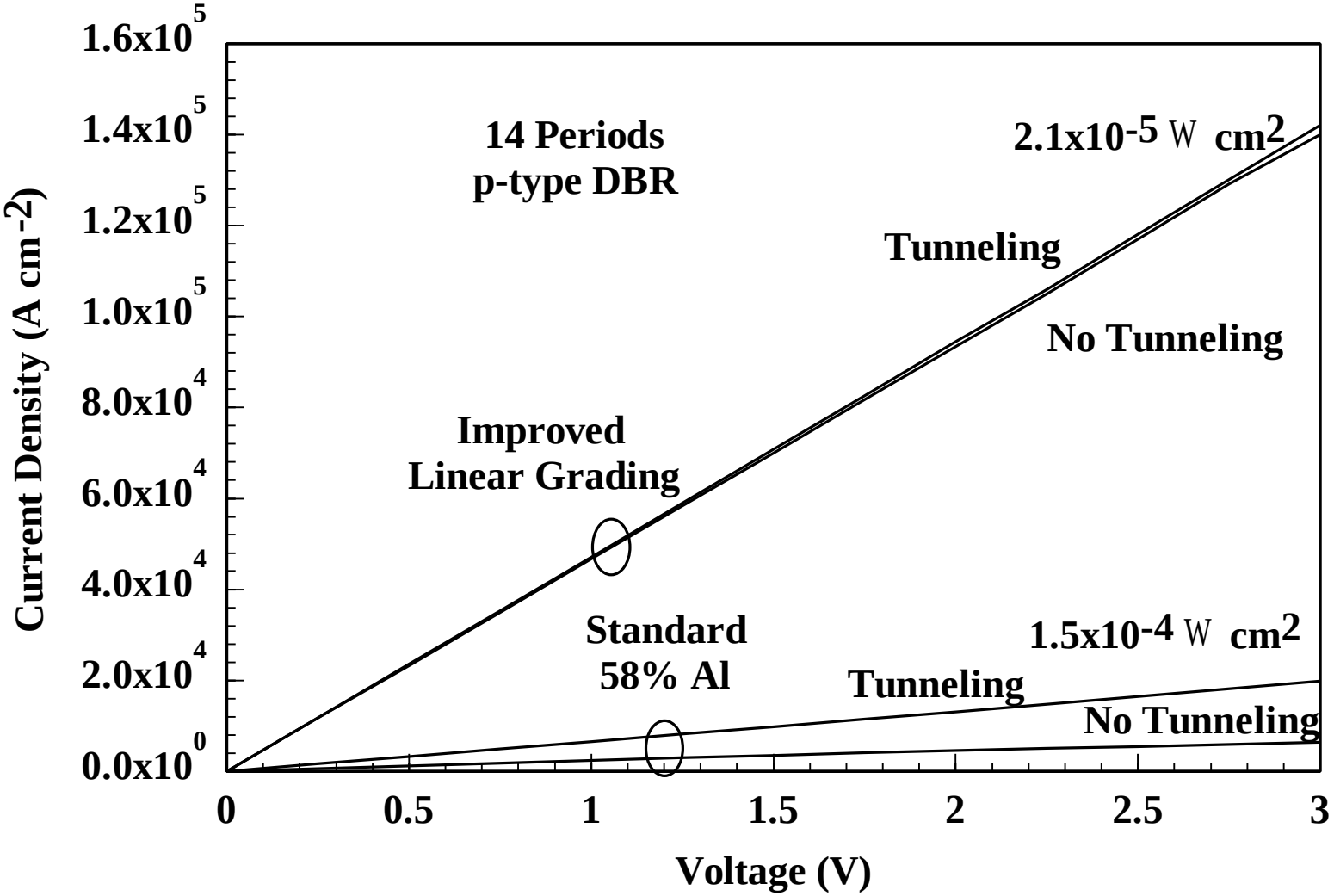
1.6x10^5
1.4x10^5
1.2x10^5
1.0x10^5
8.0x10^4
6.0x10^4
4.0x10^4
2.0x10^4
0.0x10^0
Current Density (A cm^-2)
0
0.5
1
1.5
2
2.5
3
Voltage (V)
14 Periods
p-type DBR
2.1x10^-5 W cm^2
Tunneling
No Tunneling
Improved
Linear Grading
Standard
58% Al
1.5x10^-4 W cm^2
Tunneling
No Tunneling

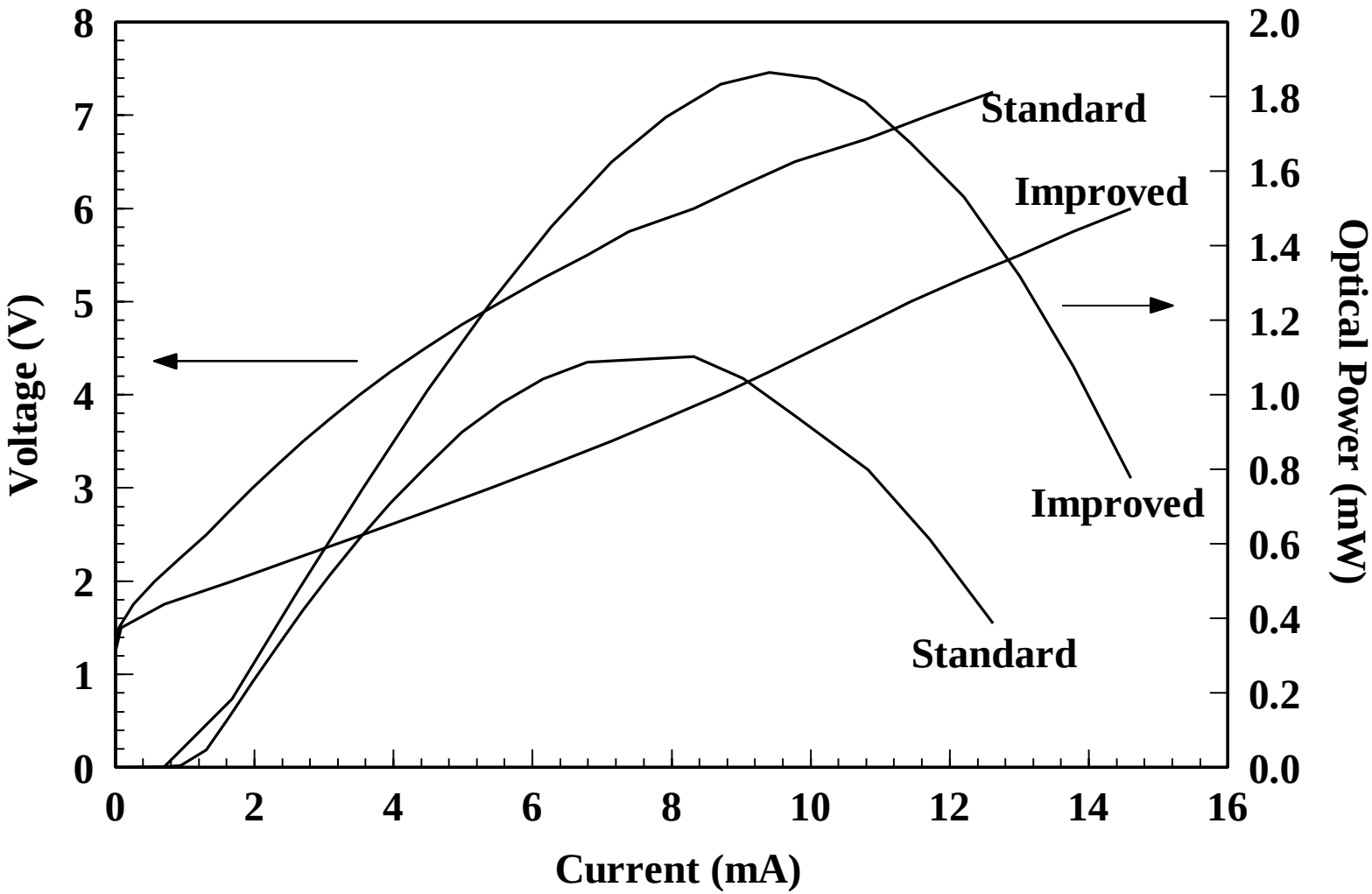
Voltage (V)
Optical Power (mW)
Current (mA)
Standard
Improved
Improved
Standard
0
1
2
3
4
5
6
7
8
0.0
0.2
0.4
0.6
0.8
1.0
1.2
1.4
1.6
1.8
2.0
0
2
4
6
8
10
12
14
16

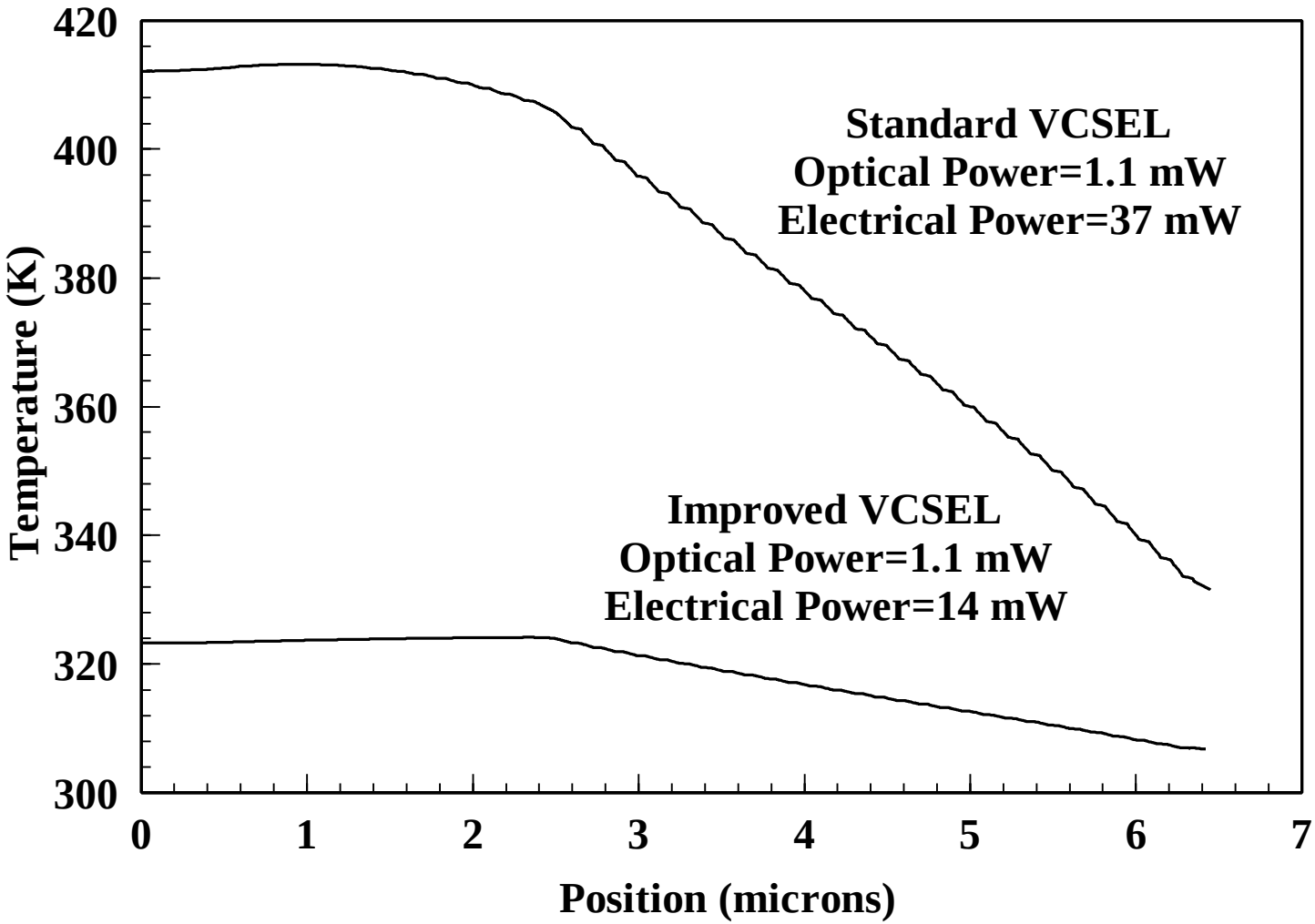
Standard VCSEL
Optical Power=1.1 mW
Electrical Power=37 mW
Improved VCSEL
Optical Power=1.1 mW
Electrical Power=14 mW
Temperature (K)
420
400
380
360
340
320
300
0
1
2
3
4
5
6
7
Position (microns)